Turbulence Statistics of Zero Pressure Gradient Turbulent Boundary Layers

By Jens M. Österlund & Arne V. Johansson

Dept. of Mechanics, KTH, SE-100 44 Stockholm, Sweden

To be submitted

Single-point turbulence statistics are here reported for zero pressure-gradient boundary layers at Reynolds numbers based on the momentum thickness in the range $2530 < Re_\theta < 27300$. The experiments were performed in the MTL wind-tunnel at the Department of Mechanics at KTH in Stockholm. A seven m long flat plate was mounted in the test section and the experiments were performed at 5 different streamwise positions. The velocity was measured using hot-wire techniques and the mean wall shear stress was determined using oil-film interferometry. Reynolds number dependence of the statistical quantities and probe size effects are discussed.

---

1. Introduction

This paper presents an experimental study of the structure single-point turbulence statistics in zero-pressure-gradient turbulent boundary layers and Reynolds number effects. The Reynolds number in typical applications with boundary layer flow are often several orders of magnitude larger than what is possible to achieve in direct numerical simulations or even compared to what is achievable in most wind-tunnels. Therefore, there is a gap in Reynolds number between practical applications and the experiments which form the basis for our knowledge of turbulence and turbulence modeling. Experiments at high Reynolds number is therefore of primary importance to reveal Reynolds number trends that might have a large influence in many fluid dynamic applications. Recent reviews of Reynolds number effects in wall-bounded shear flows was made by Gad-el-Hak & Bandyopadhyay (1994) and more specifically on zero pressure-gradient boundary layer flow by Fernholz & Finley (1996). Since the publication of the reviews two more experimental studies was published by Smith (1994) and Hites (1997). For low Reynolds numbers results from direct numerical simulations have become available starting with the simulation by Spalart (1988) followed by *e.g.* Skote *et al.* (1998).

The quest for high Reynolds number data is restrained by the availability of large size wind-tunnels but also by the demand for miniaturized flow sensors imposed by the small scales at high Reynolds numbers. In the present experiment a large effort has been put into the design and manufacturing of miniaturized hot-wire sensors, as well as their accurate positioning in the boundary layer.

2. Experimental Set-up

The experiments were performed in the MTL wind-tunnel at KTH. A seven meter long flat plate was mounted in the test section. The plate is a sandwich construction of aluminum sheet metal and square tubes in seven sections plus one flap and one nose part. The flap is 1.5 m long and is mounted in the first diffuser. This arrangement makes it possible to use the first 5.5 m of the plate for the experiment. The plate rests on two longitudinal beams running along the whole test section. The beams can be adjusted to make the plate flat to within ± 0.5 mm. The upper and lower walls of the test section can be moved to adjust the pressure distribution along the plate. The maximum variation in mean velocity distribution along the boundary layer plate was $\pm 0.15\%$. The boundary layer was tripped at the beginning of the plate and the two dimensionality of the boundary layer was checked by measuring the spanwise variation of the wall shear stress τ_w. The maximum spanwise variation in shear velocity $u_\tau = \sqrt{\tau_w/\rho}$ was found to be less than $\pm 0.7\%$. The MTL wind tunnel was designed with low disturbance level as the primary design goal and the extreme flow quality of the MTL wind-tunnel was demonstrated by Johansson (1992). For instance, the streamwise turbulence intensity was found to be 0.02%. The air temperature can be controlled to within ± 0.05 °C, which was very important for this study since the primary measurement technique was hot-wire anemometry.

One of the plate sections was equipped with two circular inserts, one for a plexiglass plug where the measurements took place, and one for the traversing system. The traversing system was fixed to the plate to minimize any vibrations and possible deflections. The positioning of the probes needs to be extremely accurate since at high Reynolds numbers the viscous (wall) scale is less than 10 μm. The distance to the wall from the probe was determined by a high magnification microscope. In addition the wall distance was measured using a laser distance meter placed under the plate looking at the probe through the plexiglass plug. The accuracy of the laser distance meter was $\pm 1\mu$m. This system made it possible to monitor the probe also with the tunnel running. It was also possible to detect probe vibrations since the frequency response of the system was 10 kHz. The absolute error in the determination of the wall distance was within $\pm 5\mu$m.

The ambient conditions were monitored by the measurement computer during the experiments using an electronic barometer and thermometer (FCO 510 from Furness Ltd., UK). The reference conditions used in the calibration of the

probes were determined using a Prandtl tube in the free-stream directly above the measurement station. The pressure and temperature were again monitored at all times during the experiments using a differential pressure transducer and a thermometer connected directly to the measurement computer. The accuracy of the pressure measurement was 0.25 % and the accuracy of the temperature measurement was 0.02 °C.

Constant temperature hot-wire anemometry was used in all velocity measurements. All hot-wire probes were designed and built at the lab. Three sizes of single-wire probes were used in the experiments with wire diameters of: 2.5, 1.27 and 0.63 μm. Two other types of probes were also used: X- and V-wires. The wire diameter for the X- and V-wire probes was 1.27 μm. The wire-separation for the X-wire probe was 220 μm and the wire length about 300 μm. The wires were placed at an angle of about $\pm 45°$ to the mean flow angle. The V-wire probe had two wires placed at $\pm 45°$ to the mean flow lying in the same horizontal plane. The wire length was 300 μm and the maximum spanwise extent was about 500 μm. The anemometer system (AN1003 from AA lab systems, Israel) had a built-in signal conditioner and the signals from the anemometer were digitized using an A/D converter board (A2000 from National Instruments, USA) in the measurement computer. The A/D converter has 12 bit resolution and four channels which could be sampled simultaneously at rates up to 1 MHz divided by the number of channels used.

The complete experiment was run from a program on the measurement computer which controlled the tunnel velocity, the positioning of probes, digitization of the anemometer signals, monitoring of the pressures and the temperature. This made it possible to design experiments which could be performed relatively quickly since monotonous work with moving probes and registering the parameters involved was done rapidly by the computer. For the double wire measurements the time to perform an measurement was also reduced by streaming the data directly to the hard disk and evaluating only a small amount of the data, for monitoring purpose, during the measurement. This made the time to carry out an experiment very close to the total sampling time plus the traversing time. The main reason for all the effort put into this was to minimize the effect of drift which is always present in any anemometer system. Furthermore, the lifetime of probes with 0.63 μm wire diameter was only a couple of hours at the higher tunnel speeds and to manage both calibration and the measurement before the wire breaks one has to avoid any unnecessary delays. To further reduce drift all instruments were always on and the tunnel was kept running for at least three hours before the experiment was performed. For a detailed description of the experiment, see paper 8.

3. Skin Friction Measurements

Accurate determination of the skin friction in the zero pressure gradient boundary layer is a very difficult task. Only a few independent methods are available:

the floating element *i.e.* measurement of the tangential force of a part of the wall and using the definition of the stress $\tau_w = F/A$, where F is the force on the floating element and A is the area of the floating element, measurement of the velocity gradient at the wall and using $\tau_w = \mu \partial \overline{U}/\partial y$, where μ is the dynamic viscosity of the air, and oil-film interferometry. In oil-film interferometry the deformation of a thin film of oil is registered in time using optical interferometry. It is an independent method since it does not need to be calibrated. Only properties of the oil must be known.

Oil-film interferometry was used to determine the skin friction in this experiment and the adapted method is described by Fernholz *et al.* (1996). Results and comparisons with other experiments and other methods can be found in paper 2 and Österlund *et al.* (1999).

A fit to c_f by a variant of the logarithmic skin friction law (Equation (6)), namely

$$c_f = 2\left[\frac{1}{\kappa}\ln(Re_\theta) + C\right]^{-2}, \tag{1}$$

was made for each of the data sets and the friction velocity used in scaling the data was then calculated as $u_\tau = U_\infty (c_f/2)^{1/2}$. The value of the von Kármán constant determined in this way was $\kappa = 0.384$ and the additive constant was found to be $C = 4.08$, see Österlund *et al.* (1999).

4. Mean Flow Characteristics

The mean flow characteristics of the turbulent boundary layer, with a focus on the properties of the overlap region, were carefully investigated and are reported in paper 2. The behavior of the boundary layer confirms the traditional two-layer theory with a logarithmic mean velocity profile in the overlap region.

The outer and inner length scales are chosen as δ, the boundary layer thickness and the viscous length $l^* = \nu/u_\tau$, where $u_\tau = \sqrt{\tau_w/\rho}$ is the friction velocity, τ_w is the skin friction and ρ is the density of the air. Dimensional analysis gives the scaling of the velocity in the inner part of the boundary layer, the law-of-the-wall

$$\overline{U}^+ = \frac{\overline{U}}{u_\tau} = f\left(y^+\right); \quad \overline{y}^+ = \frac{y u_\tau}{\nu} \tag{2}$$

and the scaling in the outer part of the boundary layer, the defect law

$$\frac{U_\infty - \overline{U}}{u_\tau} = F(\eta) \quad \eta = \frac{y}{\delta}. \tag{3}$$

At high Reynolds numbers there is a region of overlap, $\nu/u_\tau \ll y \ll \delta$, between the two scalings where both are simultaneously valid. Matching (Millikan 1938) the law-of-the-wall (2) and the defect law (3) in the traditional manner gives

the logarithmic overlap region: in inner variables,

$$\overline{U}^+ = \frac{1}{\kappa}\ln\left(y^+\right) + B \tag{4}$$

and in outer variables

$$\frac{U_\infty - \overline{U}}{u_\tau} = -\frac{1}{\kappa}\ln\left(\eta\right) + B_1. \tag{5}$$

Equations (4) and (5) also relate the skin friction with the Reynolds number and can be combined to give the logarithmic skin friction law

$$\frac{U_\infty}{u_\tau} = \frac{1}{\kappa}\ln\left(\frac{\delta u_\tau}{\nu}\right) + B + B_1. \tag{6}$$

A simplified variant of the logarithmic skin friction law, see equation 1, was fitted to the oil-film experiments and later used in the scaling of the experiments.

In figures 1 and 2 the mean velocity profiles from single-wire measurements in the Reynolds number range $2500 < Re_\theta < 27700$ are shown in inner and outer scaling. Excellent agreement with the above theoretical result is seen also over this wide Reynolds number range. Also shown in the figures are the logarithmic laws with the newly determined values of the log-law constants $\kappa = 0.38$, $B = 4.1$ and $B_1 = 3.6$. The value of the constant B_1 depends on the choice of outer scale. In this paper we use the Rotta-Clauser lengthscale $\Delta = \delta^* U_\infty / u_\tau$, Rotta (1950). As described in paper 2 the Rotta-Clauser length scale is preferred, compared to the other available and equivalent scalings, because it is experimentally more well defined. One should keep in mind, though, that Δ is substantially larger than the boundary layer thickness. $\Delta/\delta_{95} \approx 5.68$. The value of B_1 was determined in paper 2 using δ_{95} but can easily be transformed to the Δ-scaling by

$$B_1^\Delta = B_1^{\delta_{95}} - \frac{1}{\kappa}\log\left(\frac{\Delta}{\delta_{95}}\right), \tag{7}$$

giving the value $B_1^\Delta = 1.62$ used in figure 2.

5. Streamwise turbulence intensity and spatial resolution effects

In any investigation of turbulence statistics spatial averaging due to finite probe size must be carefully addressed. Johansson & Alfredsson (1983) made a detailed experimental investigation of spatial resolution effects for near-wall turbulence measurements and compiled data from the literature to elucidate such effects, see also *e.g.* Comte-Bellot (1976)

The measured velocity from a hot-wire probe is a weighted average over the wire length. That is, the probe will average out variations in the velocity field that are smaller than the length of the wire. Several attempts to address the

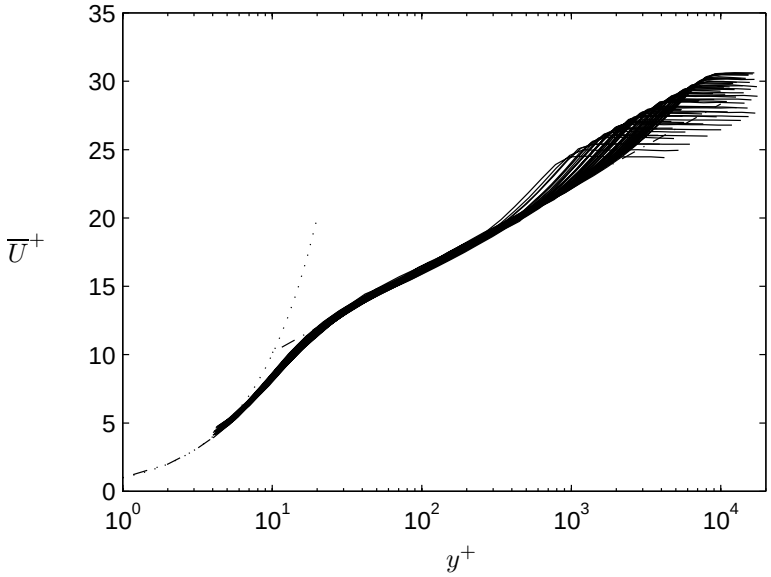

FIGURE 1. Profiles of the mean velocity in inner-law scaling. $2530 < Re_\theta < 27300$. Dash-dotted line: $\frac{1}{0.38}\ln y^+ + 4.1$.

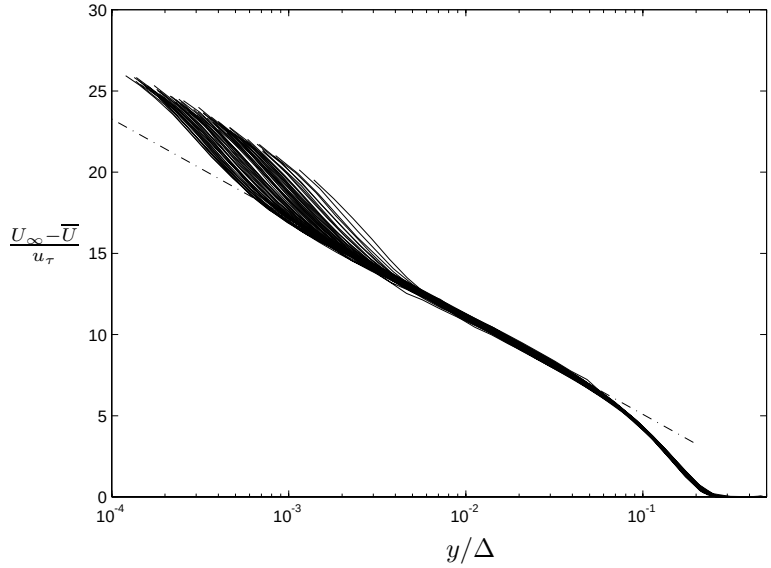

FIGURE 2. Profiles of the mean velocity in outer-law scaling. Log-law constants $\kappa = 0.38$ and $B_1^\Delta = 1.62$. $2530 < Re_\theta < 27300$

problem of spatial averaging have been reported, see *e.g.* Ligrani & Bradshaw (1987) and Willmarth & Bogar (1977).

For double wire probes Österlund (1995) showed that there is a physical limit where further minimization results in thermal crosstalk between the sensing wires that destroys the velocity signal regardless of the spatial resolution. This effect limits the size of double-wire probes to a Péclet number, based on the separation between the wires, to be larger than about 50. The Péclet number is defined as $Pe = RePr = \overline{U}\Delta_w/\chi$, where $\overline{U}$ is the mean velocity, Δ_w is the wire separation and χ the thermometric conductivity [1]. This makes it particularly difficult to design experiments in air because of the low Prandtl number (≈ 0.7). The two contradicting limits: $L^+ < 10$ and $Pe > 50$ result in the discouraging approximate limit $U^+ > 7$ or $y^+ > 10$ for double-wire probes. Considering also the very high turbulence level in the near-wall region the inner limit for accurate double-wire probes probably is larger than $50\nu/u_\tau$ for measurements in air. Note that the only solution, for double-wire probes where the thermal interaction must be negligible is to use another medium like water or oil, with Prandtl numbers of 7 and about 100, respectively. The other route for accurate measurements in the near wall region in air is instead to exploit the thermal interaction, *e.g.* by two parallel wires very close together, as done by Gresko (1988) and Österlund (1995) (see appendix). The latter showed that the Péclet number based on the separation between the wires must be smaller than about 10. The manufacturing of this type of probes where the wires must be placed less than 10 μm from each other is a severe problem, but the rapid development in micro-machining technology may solve this problem in a not too distant future.

In figures 3 and 4 the turbulence intensity $\sqrt{\overline{u^2}}/u_\tau$ is shown in inner and outer scaling for all the measurements. Clearly, it is hard to separate Reynolds number trends from effects of spatial resolution without sorting the data. The lack of scaling can largely be attributed to spatial averaging, but also Reynolds number effects are hidden in the data. We are interested in investigating Reynolds number trends and a subset of the data where $L^+ < 10$ is shown in figure 5. This of course reduces the Reynolds number span but is necessary to remove significant effects of spatial resolution. In the top diagram of figure 5 the turbulence intensities are scaled with the friction velocity and in the bottom diagram with the mean velocity. The latter represents the relative turbulence intensity, the limiting value ($y^+ \to 0$) of which is equal to the relative wall-shear-stress fluctuation intensity. The collapse is about equally good in the viscous sub-layer and the buffer region, $y^+ < 100$ for both scalings. The peak values of the absolute and relative intensities are shown in figure 6. Also shown in figure 6 are corresponding values obtained from direct numerical simulations

[1] $\chi = \kappa/\rho c_p$, where κ is the thermal conductivity, ρ the density and c_p the specific heat at constant pressure

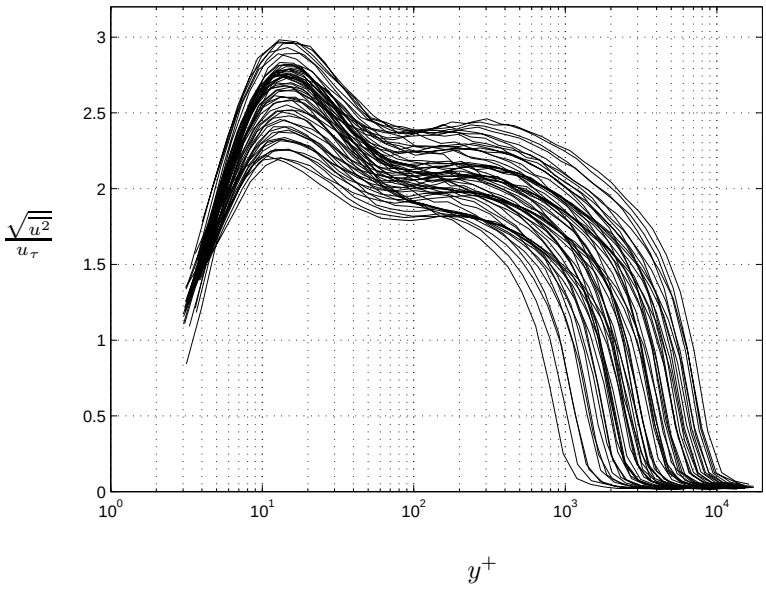

FIGURE 3. Distributions of streamwise turbulence intensity in inner-law scaling. $2530 < Re_\theta < 27300$ and $6 < L^+ < 60$.

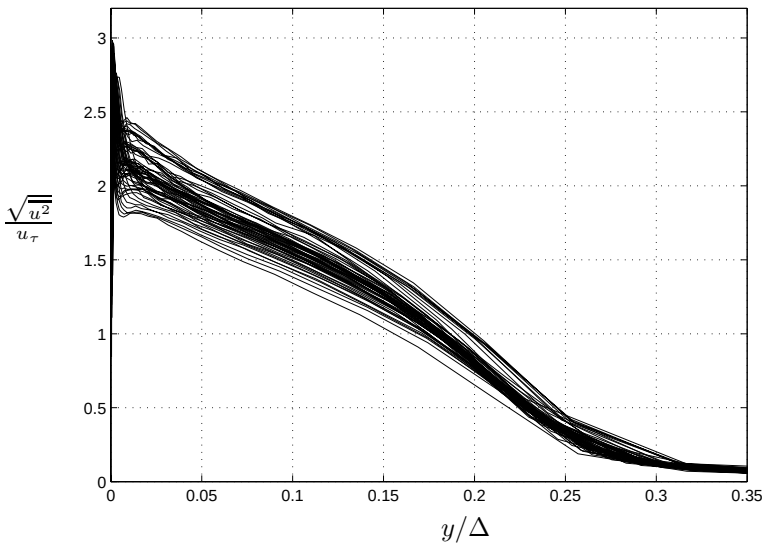

FIGURE 4. Distributions of streamwise turbulence intensity in outer-law scaling. $2530 < Re_\theta < 27300$ and $6 < L^+ < 60$.

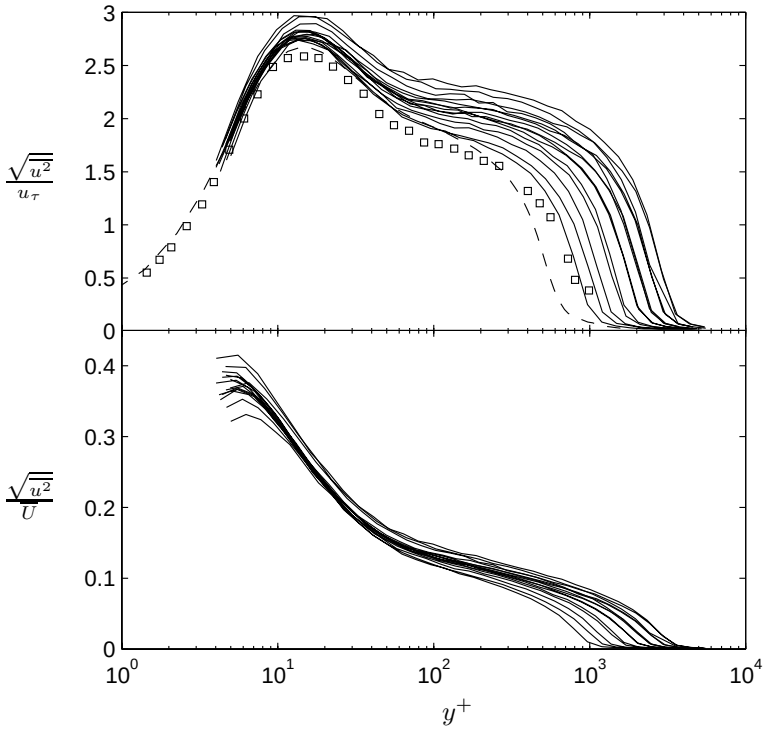

FIGURE 5. Streamwise turbulence intensity distributions using only data where $6.5 < L^+ < 10$. Inner-law scaling. $2530 < Re_\theta < 9700$. $--$: Boundary layer simulation at $Re_\theta = 1410$ by Spalart (1988). $\square$: LDV Measurements in boundary layer flow at $Re_\theta = 2420$ by Karlsson & Johansson (1988).

by Spalart (1988), Moser *et al.* (1999) and Alvelius (1999), where the first is a boundary layer simulation and the last two are channel flow simulations. One should keep in mind in the comparisons with the DNS-data that the channel flow has a somewhat different character, where Reynolds number effects on turbulence production etc. can be related to the relative influence of the pressure gradient. This can partly be seen from the integrated form of the mean flow equation. An increasing trend is visible in figure 6 for both scalings. The increase in $\sqrt{\overline{u^2}}/u_\tau$ is about 7% for the present data in this Reynolds number range but the increase in $\sqrt{\overline{u^2}}/\overline{U}$ is only about half of that. For $\sqrt{\overline{u^2}}/u_\tau$ one can observe a significant difference between the channel flow and boundary layer DNS data. The present set of experimental data smoothly extends the boundary layer DNS-results to substantially higher Reynolds numbers, with a continued increase of the maximum intensity. One could expect a levelling off

to occur at high Reynolds numbers. From the results in figure 6 it is not really possible to determine an asymptotic level of $(\sqrt{\overline{u^2}}/u_\tau)_{\max}$ but it can be judged to be at least 2.9.

The limiting value of the relative intensity at the wall is a more difficult quantity of measure. The symbols in figure 6 (lower diagram) represent evaluations at $y^+ \approx 6$. By comparisons with DNS-data we may conclude that these are approximately 10% lower than the limiting values at the wall. Hence, to enable a comparison with the DNS-data, and to give an estimation of the trend of the true limiting intensity value, a line 10% above the measured points is included in figure 6. This line is seen to represent a smooth extension from the DNS-data. At high Reynolds numbers the limiting relative intensity is estimated to be around 0.43. The effects of spatial averaging should be expected only to have marginal influence in figure 6.

The extrapolated (+10%) values in figure 6 are consistent also with measurements of the fluctuating wall shear stress by the hot-wire-on-the-wall technique (paper 5). With that technique a value of about 0.41 was found for $(\sqrt{\overline{\tau_w^2}}/\overline{\tau_w})_{\max}$ at $Re_\theta \approx 10000$. In that work also measurements with a MEMS-sensor of hot-film type are reported. The results were encouraging for this type of technique although further refinements of the sensor design can be foreseen in the near future.

6. Reynolds Stress Components

6.1. *Reynolds normal-stress*

Reynolds normal-stress distributions are presented for inner scaling in figure 7 and for outer scaling of the wall-distance in figure 8. The Reynolds number Re_θ varies from 6930 to 22500. The results for the streamwise component are taken from single-wire measurements, where the wire lengths are in the range $6.6 < L^+ < 24$. For comparison the streamwise component obtained with a X-wire probe at the highest and the lowest Reynolds number are shown as circles in figure 7, and the agreement is excellent in the outer part of the boundary layer but since the X-wire probe has a significant extension in the wall normal direction, it is not possible to measure as close to the wall as with the single wire probe.

Results for the wall-normal $\overline{v^2}$, and the spanwise component $\overline{w^2}$, are obtained with X- and V-wire probes, respectively. A behavior with constant Reynolds stresses is to be expected in the overlap region of the boundary layer. In the present data a plateau becomes visible for the higher Reynolds numbers, at least for $\overline{u^2}$ and $\overline{w^2}$. The decrease of $\overline{v^2}$ for $y^+ < 100$ for the highest Reynolds numbers can probably be ascribed to spatial resolution effects. The probe size for the four highest Reynolds numbers lies in the range $19 < L^+ < 30$. The increase in $\overline{v^2}$ near the wall is most probably an artifact caused by experimental

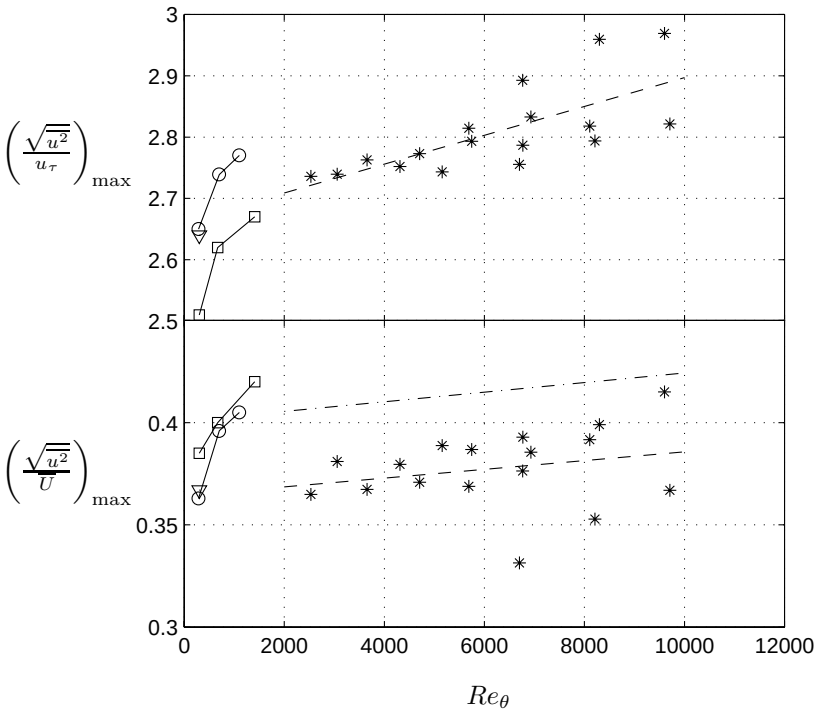

FIGURE 6. Maximum streamwise turbulence intensity. $*$: Present experiment, $6.5 < L^+ < 10$. Dashed line: linear regression to the present experiment. $\circ$: DNS of channel flow by Moser *et al.* (1999). $\square$: DNS of zero pressure gradient boundary layer by Spalart (1988). ∇: DNS of channel flow by Alvelius (1999).

errors. Also shown are results from measurements with a parallel-wire probe (Österlund 1995) at Reynolds number $Re_\theta = 14500$. It does not have the same problems in the near-wall region but possibly gives a too low value in the outer part of the boundary layer.

The strong increase in $\overline{w^2}$ near the wall is most probably an artifact due to experimental errors. One may speculate that effects of $\partial u/\partial z$ and $\partial v/\partial z$ fluctuations become of significant influence near the wall. The spanwise wire-separation of the V-probe ranges from 29 to 90 viscous length scales in figures 7 and 8.

The fact that the plateau in the Reynolds stresses only is seen for the highest Reynolds numbers is somewhat analogous to the behavior in free shear

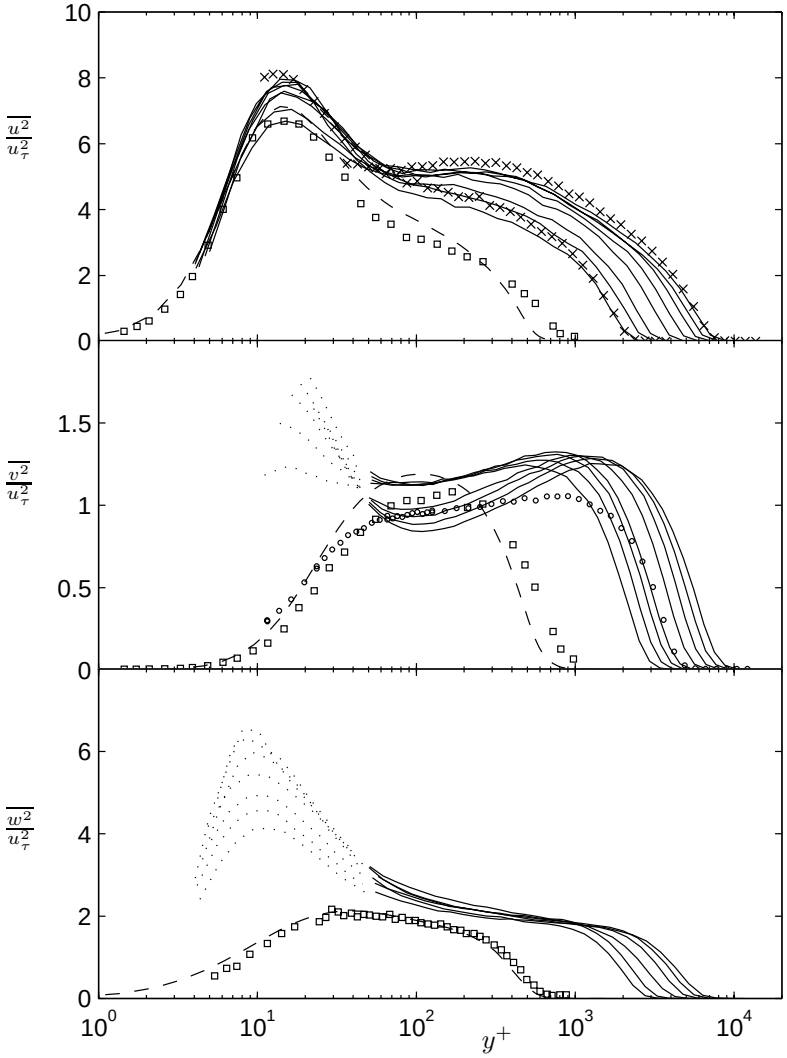

FIGURE 7. Distributions of the Reynolds normal-stress components in inner-law scaling of the wall-distance. $6930 < Re_\theta < 22500$. $\overline{u^2}$ data from a single-wire probe, $\overline{v^2}$ from a X-wire probe and $\overline{w^2}$ from a V-wire probe. $\times$: X-wire probe at Re_θ 6930 and 22500. $\circ$: Parallel-wire probe, $Re_\theta = 14500$. $--$: Boundary layer simulation at $Re_\theta = 1410$ by Spalart (1988). $\square$: LDV Measurements in boundary layer flow at $Re_\theta = 2420$ by Karlsson & Johansson (1988). Dotted parts of curves represent measured data with significant effects of wire-separation etc.

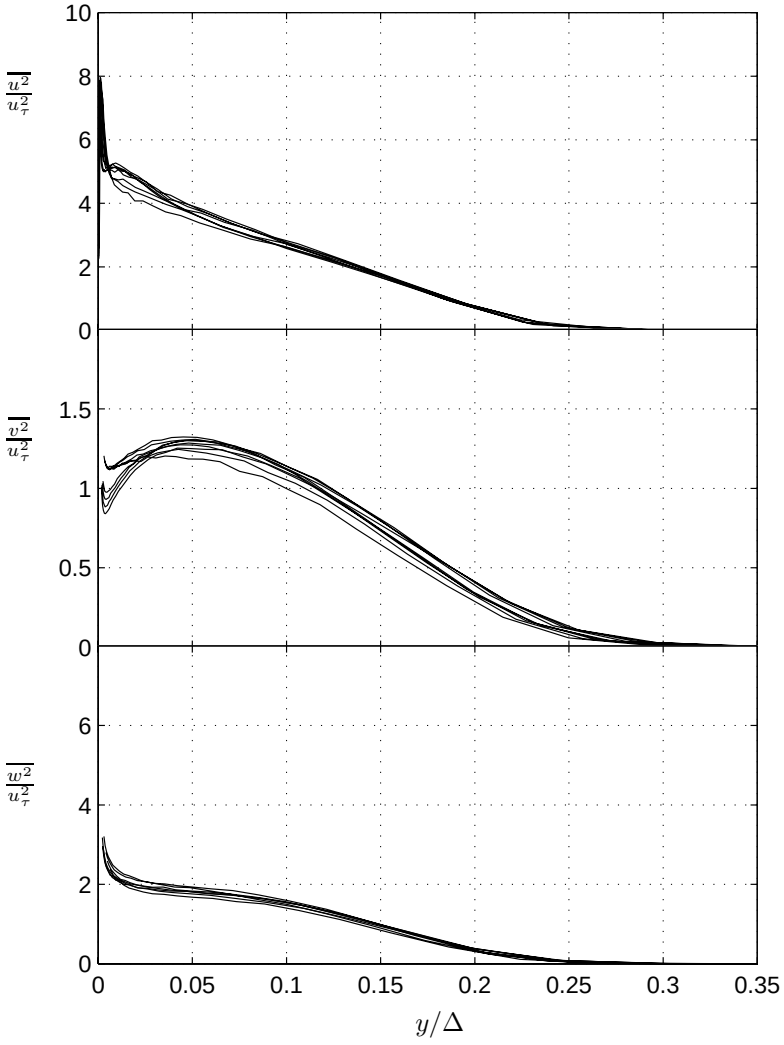

FIGURE 8. Distributions of the Reynolds normal-stress components in outer-law scaling. $6930 < Re_\theta < 22500$. Only data where $y^+ > 50$ are shown for the transverse components.

flows where a self-similar behavior of Reynolds stresses requires a substantially longer development than for the mean velocity.

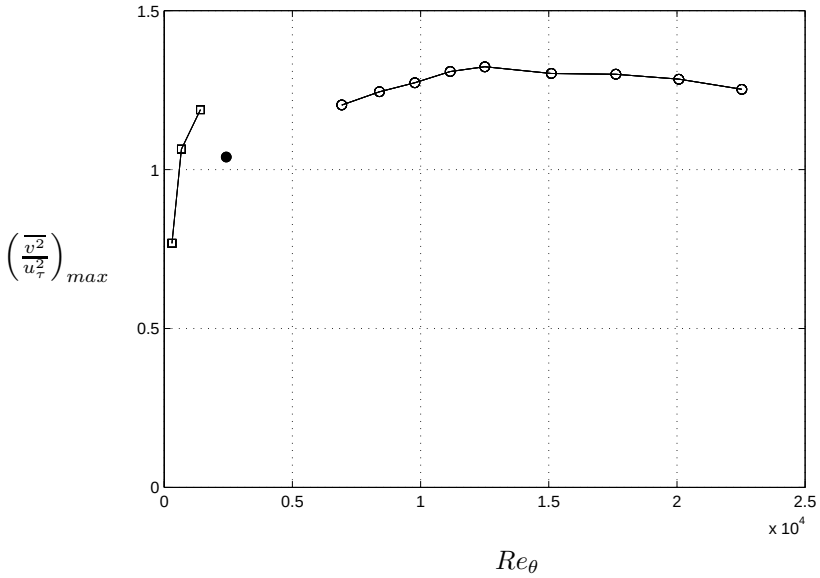

FIGURE 9. Maximum wall-normal turbulence intensity, $\left(\overline{v^2}/u_\tau^2\right)_{max}$. ○: Present data. Wire separation is $L^+ = 6$ for the low Reynolds number increasing to $L^+ = 18$ for the highest Reynolds number. □: DNS of zero pressure gradient boundary layer by Spalart (1988). •: LDV measurement by Karlsson & Johansson (1988).

The peak value of $\overline{v^2}$ is seen in figure 9 to increase with the Reynolds number in a manner similar to the variation in the peak value for $\overline{u^2}$. At the high Reynolds number end a decreasing trend is seen that is probably due to spatial averaging effects. The increase in $(\overline{v^2}/u_\tau)_{\max}$ for $Re_\theta < 13000$ seems consistent with the low Reynolds number DNS-results. Fernholz & Finley (1996) reported max-values of about 1.4 for $Re_\theta = 20920$ obtained with a probe size of about 26 in wall-units. This is in reasonable agreement with the results in figure 9.

6.2. *Reynolds shear-stress*

Distributions of the Reynolds shear-stress $\overline{uv}$ are shown in figures 10 and 11 in inner and outer scaling, respectively. Experimental errors due to the large probe size at the high Reynolds numbers gives large uncertainties of the measurements in the near-wall region, $y^+ < 200$. The Reynolds number variation of the shear-stress peak value is shown in figure 12. The peak values show an increasing trend with Reynolds number that flattens out very close to unity for Reynolds numbers above about 15000. The increasing trend at low Reynolds numbers

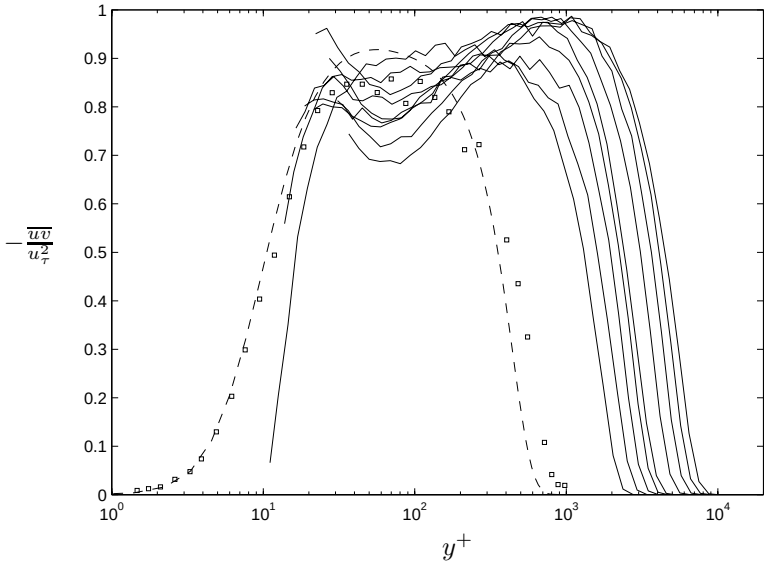

FIGURE 10. Reynolds shear stress in inner-law scaling of the wall-distance. —:Present data, from a X-wire probe, $6930 < Re_\theta < 22500$. −−: Boundary layer simulation at $Re_\theta = 1410$ by Spalart (1988). □: LDV Measurements in boundary layer flow at $Re_\theta = 2420$ by Karlsson & Johansson (1988).

also here seems consistent with the DNS-results. The shear-stress correlation coefficient is shown in figures 13 and 14. A wide region with a value of about 0.4 is observed and agrees well with earlier reported results for the correlation coefficient.

The ratio of the Reynolds shear stress to $\overline{q^2}$ (twice the kinetic energy) is sometimes referred to as the structure parameter. In eddy viscosity-based two equation models of turbulence one normally assumes this parameter to be equal to 0.15 to give the standard C_μ-value of 0.09 ($\nu_T = C_\mu k^2/\epsilon$). The 0.15-value is assumed to be valid in general for thin shear layers with production approximately balancing the dissipation (the Bradshaw assumption). The values in figure 15 are significantly higher than what would be expected from the Bradshaw assumption, especially for the highest Reynolds numbers.

The ratio of the wall-normal to streamwise turbulence intensities is shown in figure 16, and may be compared with $\sqrt{\overline{w^2}/\overline{u^2}}$ in figure 17. In the log-layer (below $y/\Delta \approx 0.03$, see figure 2) these two anisotropy parameters are roughly equal.

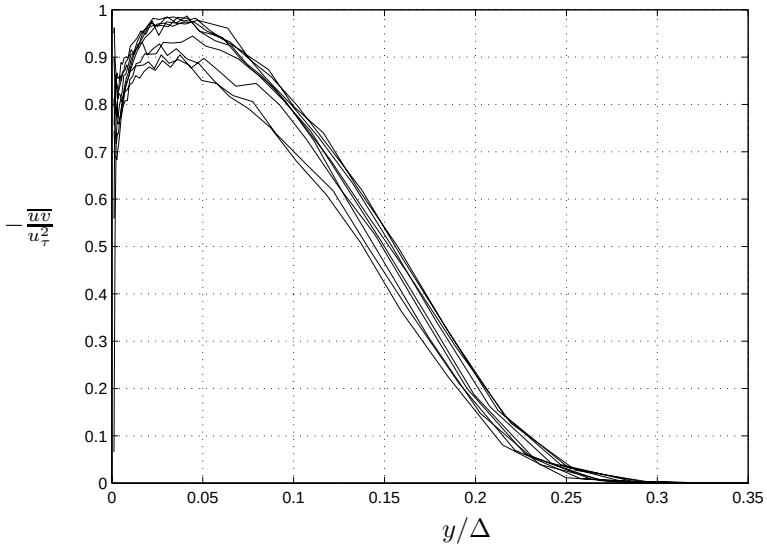

FIGURE 11. Reynolds shear stress in outer-law scaling.

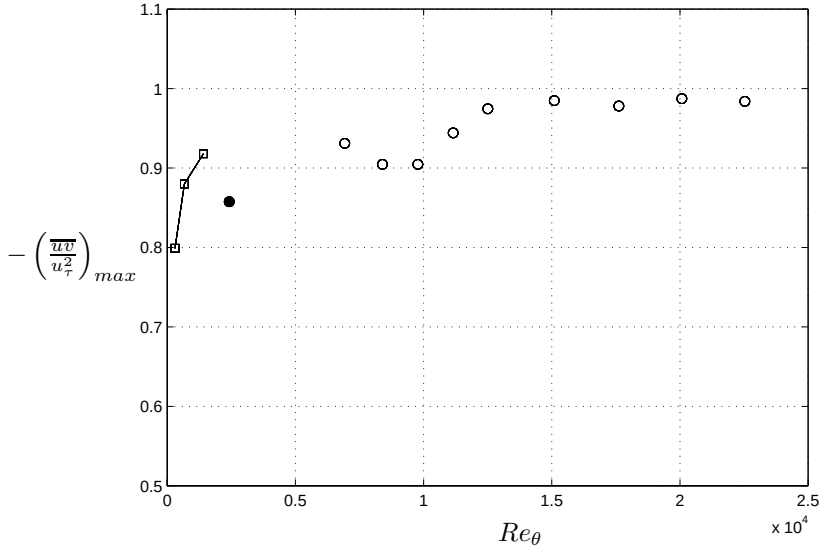

FIGURE 12. Maximum value of the shear-stress component. ○: Present data. □: DNS of zero pressure gradient boundary layer by Spalart (1988). ●: LDV Measurement by Karlsson & Johansson (1988).

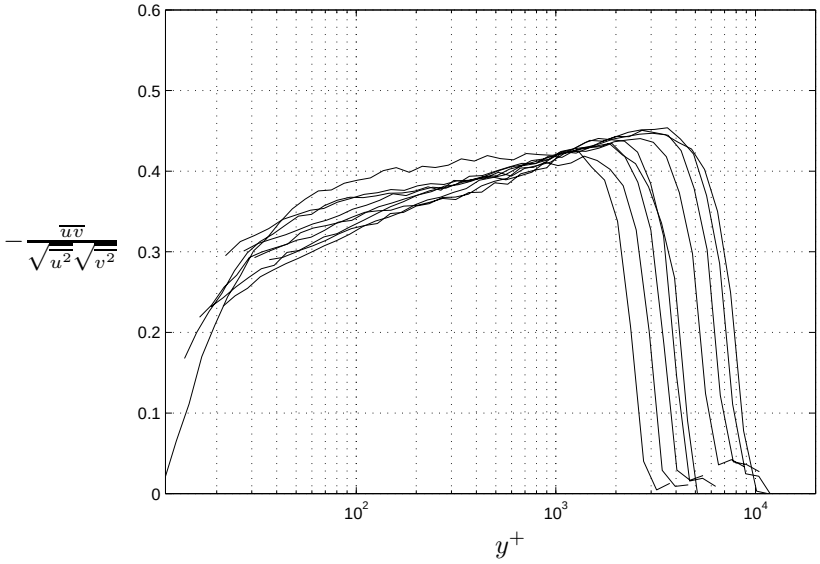

FIGURE 13. Reynolds shear stress correlation coefficient in inner-law scaling.

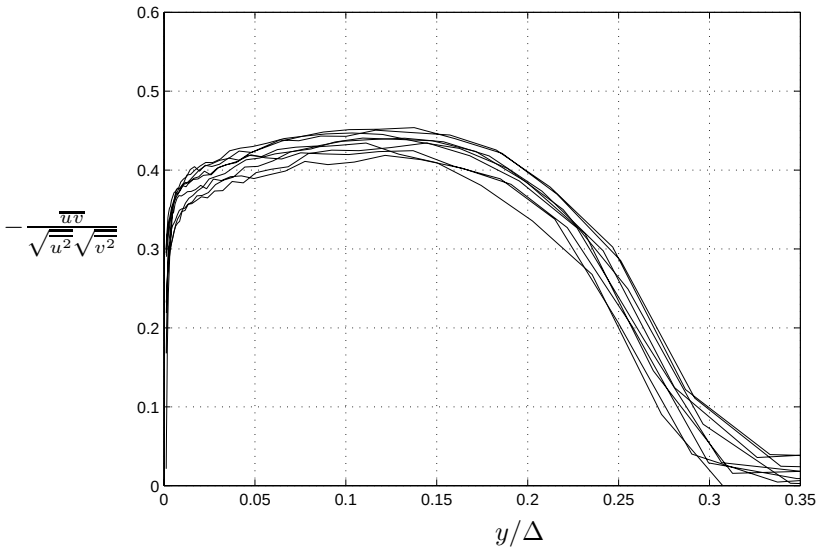

FIGURE 14. Reynolds shear stress correlation coefficient in outer-law scaling.

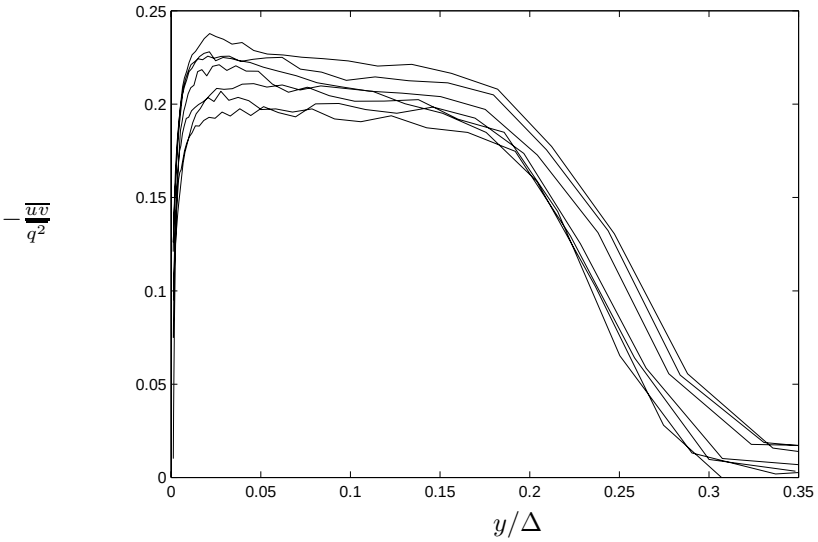

FIGURE 15. Structure parameter in outer-law scaling.

Twice the kinetic energy is shown with inner and outer y-scaling in figures 18 and 19. Also here we may observe a plateau that develops for high Reynolds numbers in the log-layer (figure 18).

The third order moment of the probability density function describes the asymmetry or skewness of the signal. Figures 20 and 21 show the skewness and flatness factors

$$S_u = \frac{\overline{u^3}}{\overline{u^2}^{3/2}} \tag{8}$$

$$F_u = \frac{\overline{u^4}}{\overline{u^2}^2}, \tag{9}$$

of the streamwise velocity component. In inner scaling an approximate collapse of the skewness and flatness profiles are observed in the whole inner layer. Correspondingly, we see a collapse with Δ-scaling in the outer part. The high values near the boundary layer edge are caused by the intermittent character of the turbulence there. One can observe that the minimum flatness value is found at the same location as that for the zero-crossing of the skewness. This position is close to that for the maximum turbulence intensity. This observation is accordance with earlier findings, see *e.g.* Johansson & Alfredsson (1982). The high flatness closer to the wall is associated with the intermittent character of strong sweep type of motions.

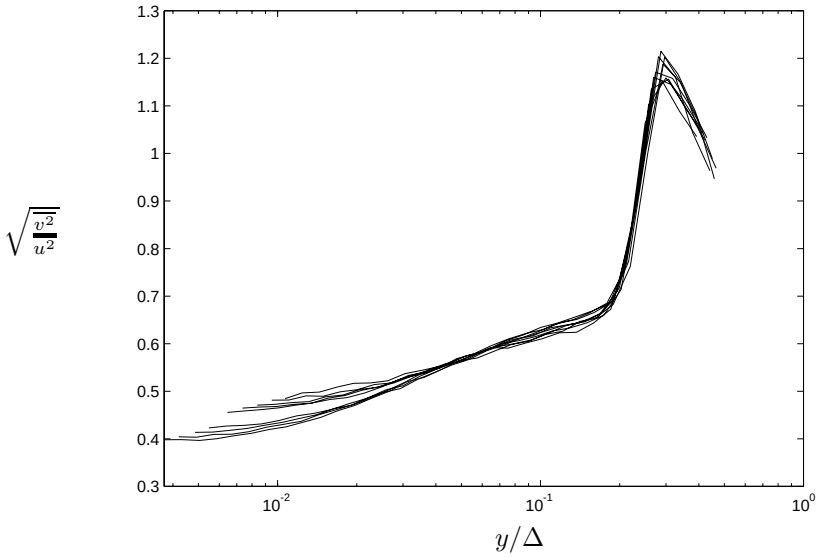

FIGURE 16. Anisotropy parameter in outer scaling.

7. Probability Density Functions

In figure 22 the probability density distributions are shown for different regions in the boundary layer. The high positive skewness value near the wall is associated with a highly asymmetric probability density distribution at *e.g.* $y^+ = 5$. The long positive tail at this position can be interpreted as being caused by sweep type of motions originating from positions far from the wall. A successive change to a negative skewness and corresponding asymmetry of the probability density distribution is seen in figure 22. To illustrate the variation of the width of the probability density distribution, an example of a mean velocity profile is shown in figure 23 together with the limits enclosing 95% of the samples.

7.1. *Joint probability densities*

The joint probability density distributions of u and v are shown in figure 24 for various distances from the wall. The direction of the main axis of the ellipse-like curves is directly related to the correlation coefficient, which in figure 24 was seen to be roughly constant over a wide region of y-values.

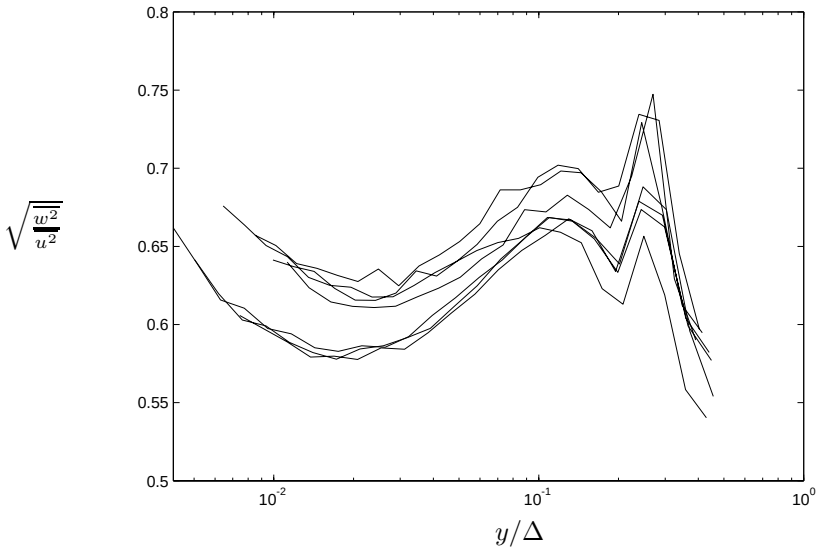

FIGURE 17. Anisotropy parameter in outer scaling.

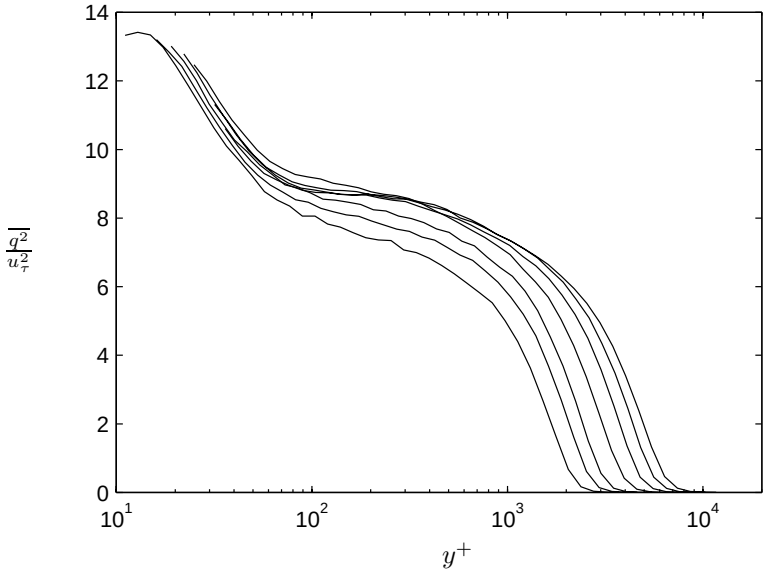

FIGURE 18. Turbulent kinetic energy, $\overline{q^2} = \overline{u^2} + \overline{v^2} + \overline{w^2}$, in inner-law scaling.

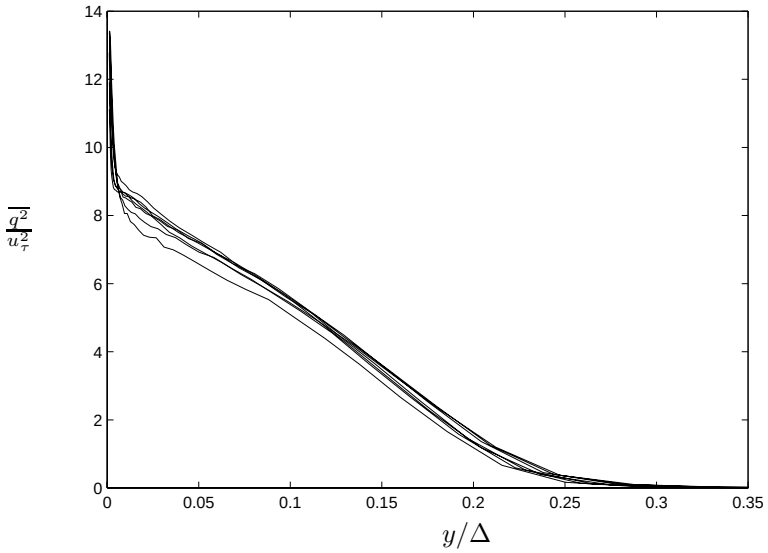

FIGURE 19. Turbulent kinetic energy, $\overline{q^2} = \overline{u^2} + \overline{v^2} + \overline{w^2}$, in outer-law scaling.

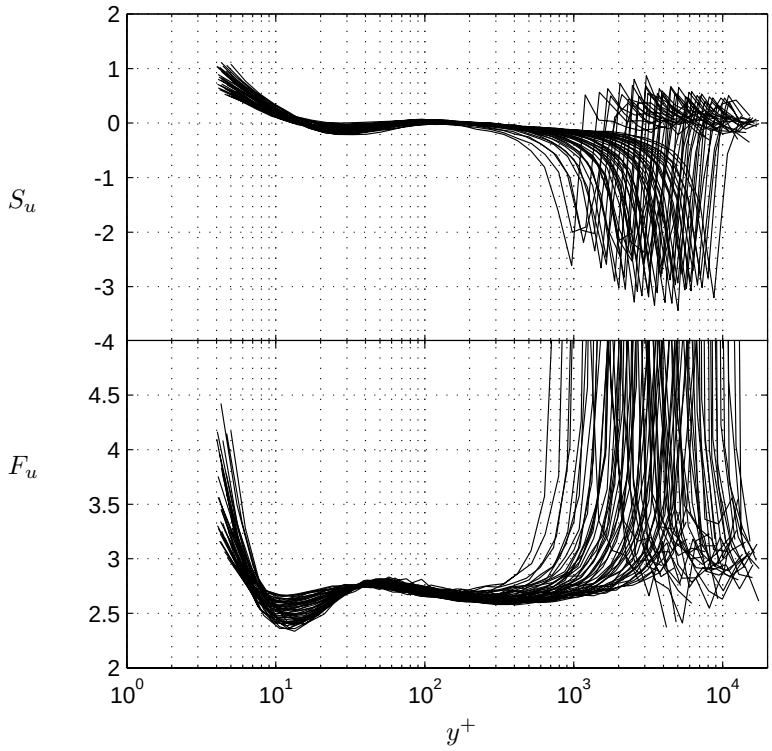

FIGURE 20. Profiles of skewness S_u and flatness F_u in inner-law scaling.

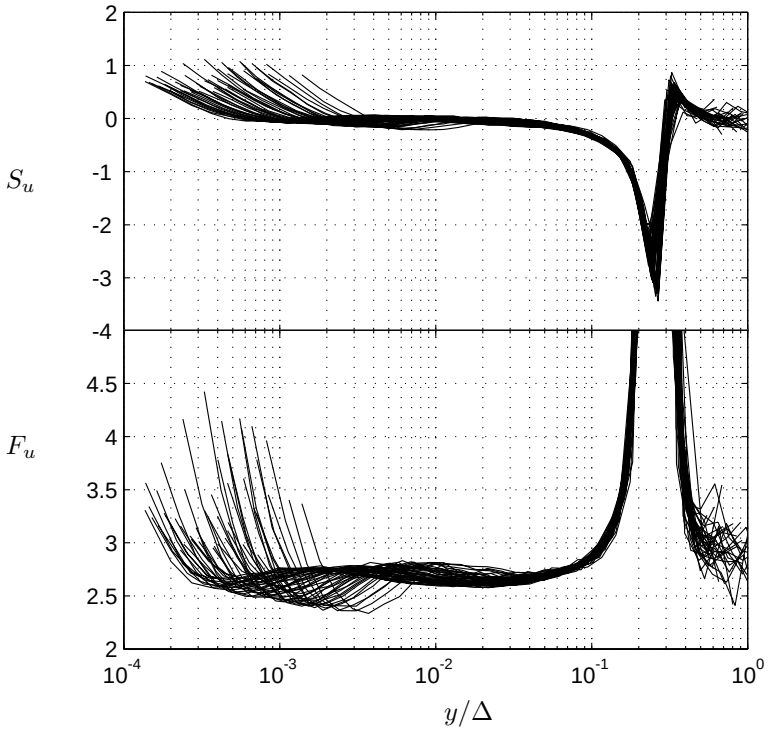

FIGURE 21. Profiles of skewness S_u and flatness F_u in outer-law scaling.

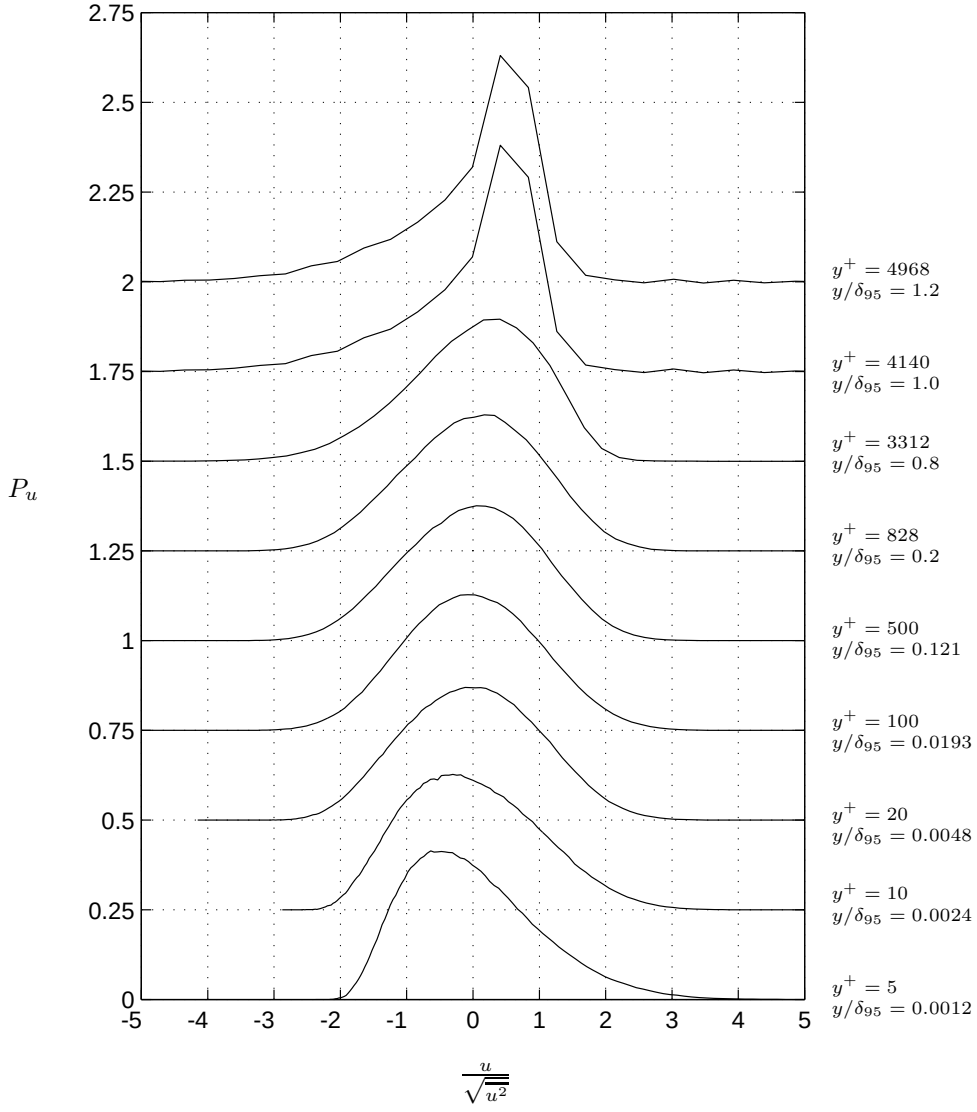

FIGURE 22. Probability density functions for the streamwise velocity at different distances from the wall. $Re_\theta = 17800$.

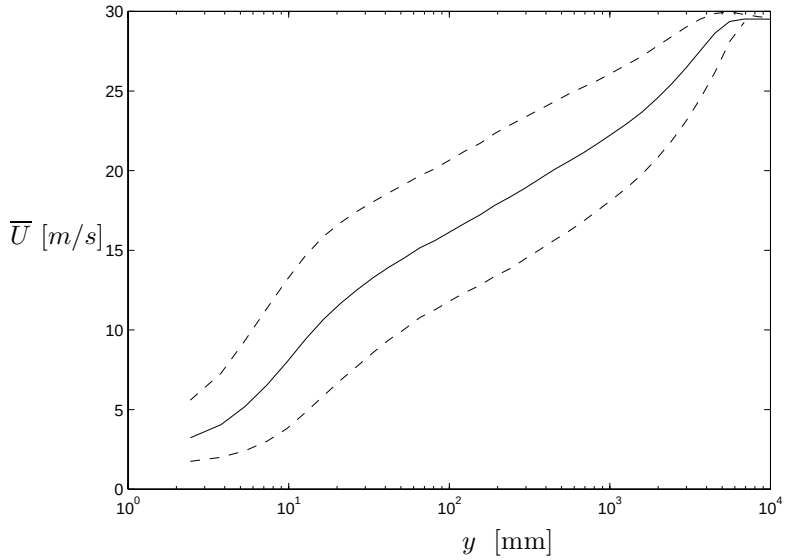

FIGURE 23. Example mean velocity profile. $Re_\theta = 17800$. Dashed line enclose 95% of the samples.

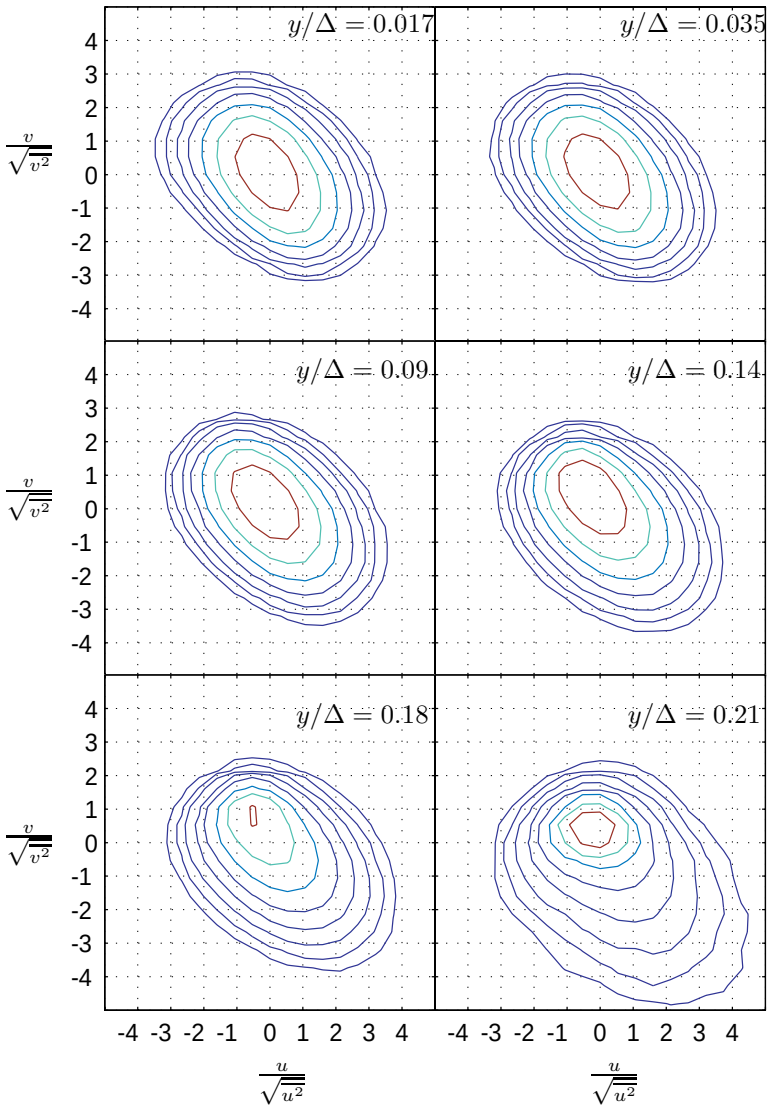

FIGURE 24. Joint-probability density functions P_{uv}, for the streamwise and wall-normal velocities at different outer-scaled distances from the wall. $Re_\theta = 26600$. Contours at ten levels with logarithmic spacing, *i.e.* $10^{\{-3,-2.66,-2.33,\ldots,0\}}$.

8. Appendix: Measurements with a Parallel-Wire Probe

8.1. *Motivation*

The use of parallel-wire probes was initiated by the need for near-wall turbulence data at high Reynolds numbers where the turbulent scales are small and the gradients are large. A conventional X-wire probe have severe problems problems in the near wall region mainly due to its large wall-normal dimension compared to the mean and fluctuating velocity gradients. Efforts have been made to miniaturize X-wire probes by several investigators, *e.g.* Willmarth & Bogar (1977). Österlund (1995) found that thermal interaction between the heated wires in X-wire probes deteriorates the signal for Peclet numbers less than 50. The idea of parallel wires is instead to utilize the thermal interaction between the wires and calibrate the probe against the velocity and angle similarly to the procedure for X-wire probes. For this to work the parallel-wire probe must always be operated in the under critical region of its transfer function, as opposed to X-wire probes who must not have any thermal interaction. The result of this is that the wires have to be placed very closely together in order to achieve a reasonably high sensitivity and a flat response to high enough frequencies. The wall normal extent of the parallel-wire probe geometry is therefore only about 1/50 or less than that of an X-wire probe. The influence from high velocity gradients at the wall is therefore much smaller.

8.2. *Probe design and calibration*

The body of the probe was built of a ceramic tube, designed for use in thermo elements, with 4 holes. The prong material was spring steel. The conical shape of the prong tips was obtained in an etching process using a bath of nitric acid (60%) applying a small voltage to speed up the etching. The delicate positioning of the prongs was done under a microscope (80x) with micro manipulating equipment gearing down the hand movement. When the prongs are fixed in position a low viscosity epoxy resin is applied. The capillary force pulls the resin into the probe body and fixes the prongs in position after hardening. To fix the prongs together outside of the ceramic body a mixture of epoxy resin and colloidal silicon was applied. Before gluing the probe together the prongs were covered by a thin layer of solder to protect it from corrosion, also the solder is used later when the platinum wires are soldered onto the prong tips. The soldering is done by putting the etched piece of the Wollastone wire in position, by use of a micromanipulator, and then heating the prong with the soldering iron a few mm away until the solder melts. The diameter of the prong edge was about 20–30 μm. The wires were soldered on the inside of the prongs to make the distance between the wires as small as possible, see figure 25. Extreme care has to be taken when positioning the prongs to assure that the wires are parallel.

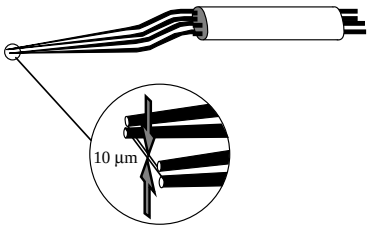

FIGURE 25. Schematic of a parallel-wire probe.

The probes were calibrated in the freestream outside of the boundary layer. The calibration of the parallel-wires was done by the same procedure used for the X-wire probes (see Paper 8). The voltages from the anemometers, the angle of attack and the speed in the freestream, measured by a pitot tube, were registered at typically 8 angles, between $-30°$ to $30°$, and 8 velocities, between 2–25 m/s.

8.3. *Parallel-wire results*

Results from measurements with the parallel-wire probes are shown in figures 26 to 29. The experimental parameters are summarized in table 1. The results for the moments of the streamwise velocity component u show good agreement with results from single wire measurements and are not reported here.

For the wall-normal Reynolds stress component $\overline{v^2}$ a reasonably good agreement with X-wire data and also DNS data by Spalart (1988) and LDV data by Karlsson & Johansson (1988) are shown in figure 26. When compared to the X-wire results it is clear that the parallel-wire probe gives accurate data much closer to the wall. In contrast to the positive results obtained for $\overline{v^2}$ the results for the Reynolds shear-stress component $\overline{uv}$ are less encouraging, as shown in figure 27. This behavior was explained by Österlund (1995) as a result of the phase shift between the u and v signals, obtained from the parallel-wire probe, as a result of finite wire separation. The solution to this problem is to reduce the wire separation even further, which is very difficult with conventional probe design techniques. The skewness and flatness factors for the wall normal velocity S_v, F_v are shown in figures 28, 29 and exhibit approximately the same results as obtained with an X-wire.

The severe difficulties with the design and construction of parallel-wires separated only a few μm was the main reason to discontinue the development of the parallel-wire probe in this study. Future MEMS technology may possess capacity to solve this problem.

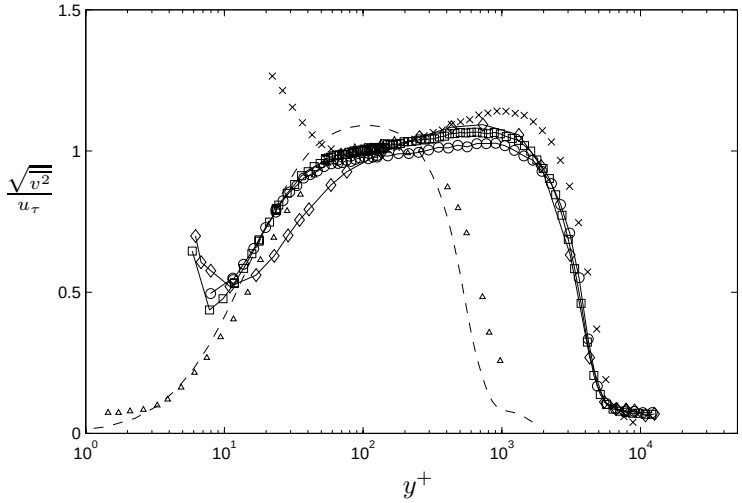

FIGURE 26. Wall normal Reynolds stress, from parallel-wire probe. For symbols, see table 1. ×: X-wire measurement, $Re_\theta = 15100$. △: LDV Measurements in boundary layer flow at $Re_\theta = 2420$ by Karlsson & Johansson (1988). −−: Boundary layer simulation at $Re_\theta = 1410$ by Spalart (1988).

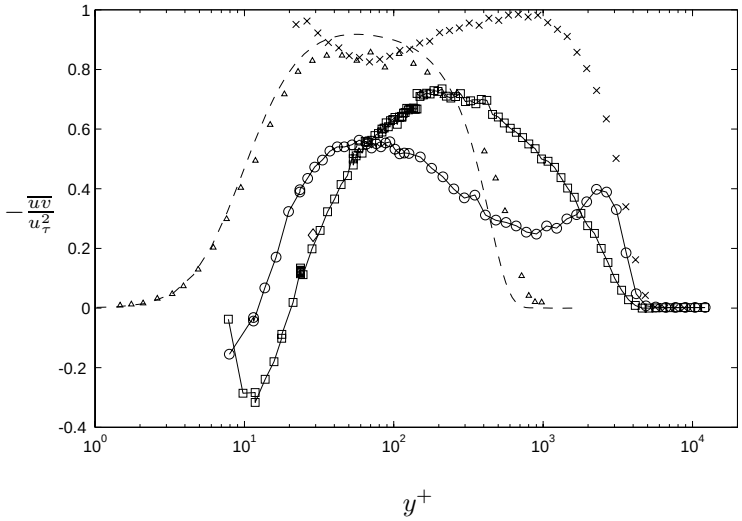

FIGURE 27. Reynolds shear stress from parallel-wire probe. For symbols, see table 1. −−: Boundary layer simulation at $Re_\theta = 1410$ by Spalart (1988). ×: X-wire measurement, $Re_\theta = 15100$. △: LDV Measurements in boundary layer flow at $Re_\theta = 2420$ by Karlsson & Johansson (1988).

Symbol		□	○	◇
d	[μm]	1.27	1.27	2.54
Δ_w	[μm]	12	5	20
l_1	[μm]	230	230	280
l_2	[μm]	270	270	360
R_{c_1}	[Ω]	16.4	16.5	5.4
R_{c_2}	[Ω]	20	19.9	6.4
x	[m]	4.5	4.5	4.5
U_∞	[m/s]	25.3	25.6	25.1
u_τ	[m/s]	0.894	0.905	0.892
Re_θ		13800	13900	13800
Δ_w^+		0.7	0.3	1.2
l^+		13.8	13.9	16.7
l/d		181	181	112

TABLE 1. Parallel-wire experiments

9. Acknowledgments

The authors wish to thank Krister Alvelius and Martin Skote for providing us with DNS data, and Alexander Sahlin who participated in the parallel-wire experiments. We wish to thank Mr. Ulf Landen and Mr. Marcus Gällstedt who helped with the manufacturing of the experimental set-up. Financial support from NUTEK and TFR is also gratefully acknowledged.

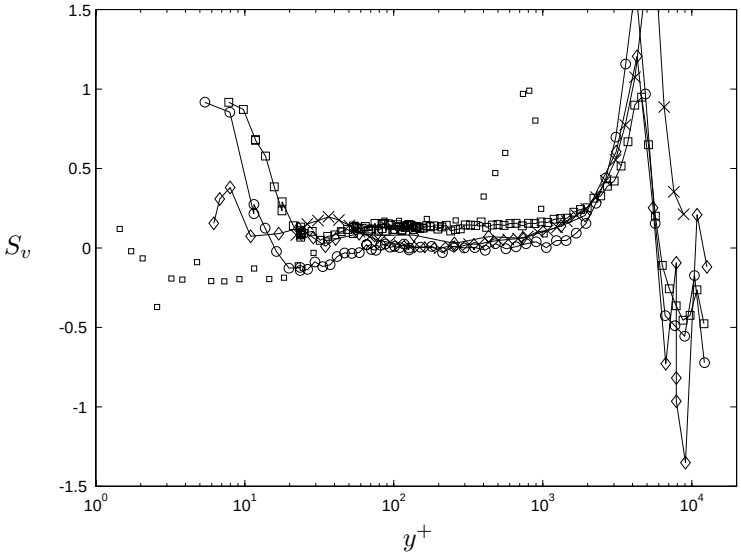

FIGURE 28. Skewness factor of the wall normal velocity, from parallel-wire probe. For symbols, see table 1. ×: X-wire measurement, $Re_\theta = 15100$. □: LDV Measurements in boundary layer flow at $Re_\theta = 2420$ by Karlsson & Johansson (1988).

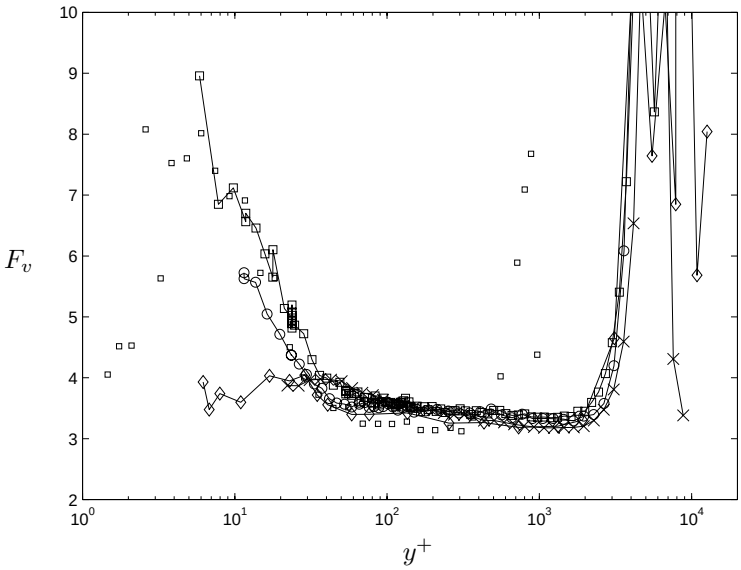

FIGURE 29. Flatness factor of the wall normal velocity, from parallel-wire probe. For symbols, see table 1. ×: X-wire measurement, $Re_\theta = 15100$. □: LDV Measurements in boundary layer flow at $Re_\theta = 2420$ by Karlsson & Johansson (1988).

References

Alvelius, K. 1999 Studies of turbulence and its modeling through large eddy- and direct numerical simulation. PhD thesis, Department of Mechanics, Royal Institute of Technology, Stockholm.

Comte-Bellot, G. 1976 Hot-wire anemometry. *Ann. Rev. Fluid Mech.* **8**, 209–231.

Fernholz, H. H. & Finley, P. J. 1996 The incompressible zero-pressure-gradient turbulent boundary layer: An assessment of the data. *Prog. Aerospace Sci.* **32**, 245–311.

Fernholz, H. H., Janke, G., Schober, M., Wagner, P. M. & Warnack, D. 1996 New developments and applications of skin-friction measuring techniques. *Meas. Sci. Technol.* **7**, 1396–1409.

Gad-el-Hak, M. & Bandyopadhyay, P. R. 1994 Reynolds number effects in wall-bounded turbulent flows. *Appl. Mech. Rev.* **47** (8), 307–365.

Gresko, Jr., L. S. 1988 Characteristics of wall pressure and near-wall velocity in a flat plate boundary layer. *Tech. Rep.* 88-2. Fluid Dynamics Research Laboratory Report.

Hites, M. H. 1997 Scaling of high-reynolds number turbulent boundary layers in the national diagnostic facility. PhD thesis, Illinois Institute of Technology.

Johansson, A. V. 1992 A low speed wind-tunnel with extreme flow quality - design and tests. In *Prog. ICAS congress 1992*, pp. 1603–1611. ICAS-92-3.8.1.

Johansson, A. V. & Alfredsson, P. H. 1982 On the structure of turbulent channel flow. *J. Fluid Mech.* **122**, 295–314.

Johansson, A. V. & Alfredsson, P. H. 1983 Effects of imperfect spatial resolution on measurements of wall-bounded turbulent shear flows. *J. Fluid Mech.* **137**, 409–421.

Karlsson, R. I. & Johansson, T. G. 1988 Ldv measurements of higher order moments of velocity fluctuations in a turbulent boundary layer. In *Laser Anemometry in Fluid Mechanics*. Ladoan-Instituto Superior Tećnico, 1096 L.C., Portugal.

Ligrani, P. M. & Bradshaw, P. 1987 Spatial resolution and measurement of turbulence in the viscous sublayer using subminiature hot-wire probes. *Experiments in Fluids* **5**, 407–417.

Millikan, C. B. 1938 A critical discussion of turbulent flows in channels and circular tubes. In *Proceedings of the Fifth International Congress of applied Mechanics*.

Moser, R. D., Kim, J. & Mansour, N. N. 1999 Direct numerical simulation of turbulent channel flow up to $Re_\theta = 590$. *Phys. Fluids* **11** (4), 943–945.

Österlund, J. M. 1995 Dynamic behavior of hot-wire probes in turbulent boundary layers. In *Advances in turbulence V* (ed. R. Benzi, (ed.)), pp. 398–402. Kluwer academic publishers.

Österlund, J. M., Johansson, A. V., Nagib, H. M. & Hites, M. H. 1999 Wall shear stress measurements in high reynolds number boundary layers from two facilities. In *30th AIAA Fluid Dynamics Conference, Norfolk, VA*. AIAA paper 99-3814.

Rotta, J. C. 1950 Über die Theorie der Turbulenten Grenzschichten. Mitt. M.P.I. Ström. Forschung Nr 1, also available as NACA TM 1344.

Skote, M., Henkes, R. & Henningson, D. 1998 Direct numerical simulation of self-similar turbulent boundary layers in adverse pressure gradients. In *Flow, Turbulence and Combustion*, , vol. 60, pp. 47–85. Kluwer Academic Publishers.

Smith, R. W. 1994 Effect of reynolds number on the structure of turbulent boundary layers. PhD thesis, Department of Mechanical and Aerospace Engineering, Princeton University, USA.

Spalart, P. R. 1988 Direct simulation of a turbulent boundary layer up to $Re_\theta = 1410$. *J. Fluid Mech.* **187**, 61–98.

Willmarth, W. W. & Bogar, T. J. 1977 Survey and new measurements of turbulent structure near the wall. *Phys. Fluids* **20** (10), 9–21.